2026 IEEE International Conference on Robotics and Automation (ICRA 2026)
June 1-5, 2026. Vienna, Austria

Learning-Based Torque Estimation for Harmonic Drive Actuators

Chun-Hung Huang, Chun-Wei Chen, and Chao-Chieh Lan, *Senior Member, IEEE*

***Abstract*—Accurate torque estimation in robotic actuators with harmonic drives is challenging due to nonlinear hysteresis and efficiency losses, often necessitating external torque sensors. This paper presents a learning-based torque estimation method that leverages encoder-derived features and mechanical compliance to enhance estimation accuracy without additional sensors. An actuator design incorporating a compliant helical tube provides deformation features that are effectively modeled using a Long Short-Term Memory (LSTM) network. Unlike conventional calibration or parametric approaches, the proposed framework captures nonlinear, history-dependent behaviors across varying operating conditions. Experimental evaluations demonstrate that compliant tubes significantly improve estimation accuracy compared with designs using stiffer or even rigid tubes, enabling more robust generalization under different torques, impedance modes, and stiffness levels. These results highlight the importance of co-designing actuator compliance and deep learning models to achieve reliable and compact torque estimation for harmonic drive actuators.**

***Index Terms*—Deep learning, long short-term memory (LSTM), harmonic drive actuators, series elastic actuator, torque estimation.**

I. Introduction

Torque sensing is a key factor for collaborative interaction and safe control in robotic actuators. Various sensor-based solutions, such as strain-gauges [1-2] or multi-axis force sensors [3], have been widely adopted, but incorporating them often increases mechanical complexity and limits actuator compactness. To enable more compact actuator designs, series elastic actuators (SEA) can be used to estimate actuator output torque from the deformation of internal compliant elements measured using encoders [4]. This approach also simplifies torque control by transforming it into a displacement control problem. The compliance of SEAs not only enables torque sensing but also provides energy storage and shock tolerance for safe interaction. Rotary SEAs in robotic actuators typically use planar [5-7] or tube flexures [8-10], which differ in stiffness, torque capacity, and structural complexity depending on the applications. In addition, tube-based designs offer a compact form, higher torque capacity, and simpler integration with other components. These designs exhibit continuous and predictable deformation under load, producing features that can be readily measured by encoders. In SEA-based actuator designs, harmonic drives are often employed to provide high torque output and maintain output stiffness [8]. However, accurate torque estimation in actuators with harmonic drives remains particularly challenging.

Chun-Wei Chen is with the Department of Mechanical Engineering, National Cheng Kung University, Tainan, Taiwan. Chun-Hung Huang and Chao-Chieh Lan are with the Department of Mechanical Engineering, National Taiwan University, Taipei, Taiwan. (Corresponding author email: lancc@ntu.edu.tw).

Harmonic drives are widely adopted in robotic actuators [1-2, 4, 11] owing to their compact size, high gear ratio, and zero backlash. Despite these advantages, the flex spline deformation and transmission errors give rise to hysteresis effects, which manifest as history-dependent behavior. As a result, actuator output features, such as position, velocity, and torque, depend not only on the current input but also on previous states, making it difficult to have accurate modeling under varying control conditions.

Common methods for modeling hysteresis effects, including curve fitting and parametric modeling [12-14], often struggle to fully capture actuator dynamics, especially under changing external loads. These approaches usually operate under fixed conditions, making it difficult to account for nonlinear and history-dependent behaviors. In contrast, learning-based methods offer a better modeling strategy by directly estimating hysteresis effects from actuator data, effectively capturing both nonlinear and history-dependent behaviors across different operating conditions.

While conventional feedforward neural networks demonstrate the potential of learning-based torque estimation, they often process only real-time data and lack memory of prior system states. For instance, the backpropagation neural network (BPNN) method [15] was applied to estimate torque in a harmonic drive actuator using motor current and dual-encoder measurements. However, because only instantaneous data were considered, the model could not retain information about previous behavior. Another learning-based torque estimation method was proposed for cycloidal gear actuators [16]. In [16], a Gated Recurrent Unit (GRU) was trained using encoder signals such as velocity and acceleration. As a type of recurrent neural network (RNN), the GRU employs gating mechanisms to capture temporal dependencies in sequential data, effectively modeling the dynamic relationships between past and present input features and external torque. Compared with conventional feedforward networks, the GRU-based model achieved higher accuracy in estimating torque. While GRUs are effective for general sequential modeling, other RNN architectures, such as Long Short-Term Memory (LSTM) networks, provide enhanced capabilities for representing history-dependent behaviors such as hysteresis. LSTMs, with their built-in memory cells and flexible gating structures, can selectively retain or discard relevant information over extended time horizons. For harmonic drive actuators, these properties allow LSTMs to leverage time-series features derived from encoder measurements, such as deformation or angular motion, to achieve accurate and robust torque estimation under varying operating conditions.

Existing learning approaches have primarily been applied to geared actuators, demonstrating improvements in torque estimation. However, little attention has been given to how the geartrain itself might be mechanically redesigned to

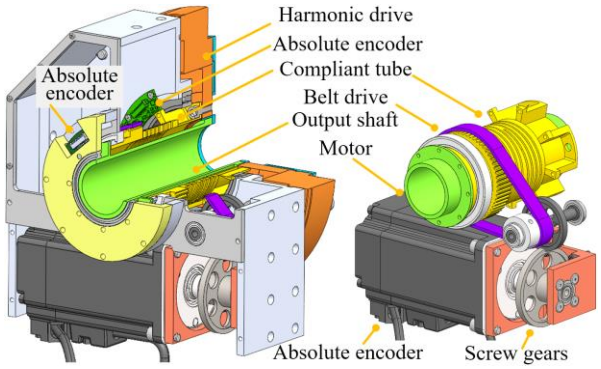

Fig. 1. (a) Cutaway view and (b) transmission components of the robotic actuator

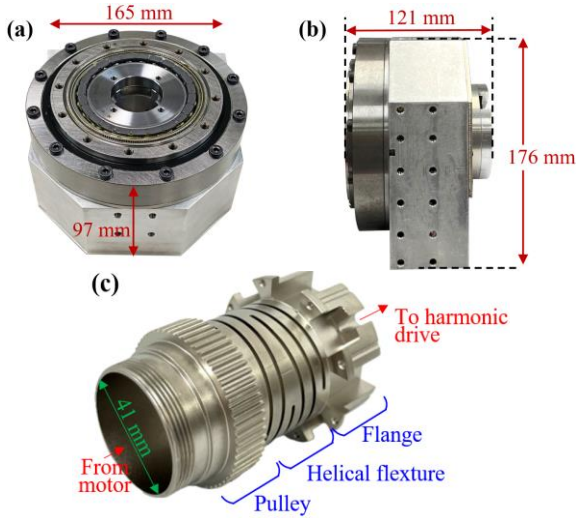

Fig. 2. Robotic actuator prototype: (a) Front view (b) Side view (c) Compliant tube

enhance learning performance, enabling more accurate torque estimation at faster convergence speeds.

This paper develops a learning-based torque estimation model for harmonic drive actuators using an LSTM framework. By incorporating a compliant helical tube into the drivetrain, deformation features measurable by encoders are introduced to improve learning performance and estimation accuracy. The actuator thereby functions as a torque sensor without additional hardware, enabling torque detection under both high-impedance and zero-impedance modes. The proposed framework is validated through experiments across varying external torques, impedance conditions, and tube stiffnesses, demonstrating enhanced accuracy, robustness, and training efficiency.

In what follows, the design and modeling of the proposed actuator are introduced in Sec. 2. Sec. 3 presents the LSTM-based deep learning framework for torque estimation, including the network architecture and the training process. The accuracy of the torque estimation model with different encoder selections is analyzed in Sec. 4, followed by evaluations of generalization under various external torques, impedance conditions, and tube stiffnesses in Sec. 5. Finally, conclusions are made in Sec. 6.

II. Actuator Design and Modeling

2.1 Prototype of the actuator

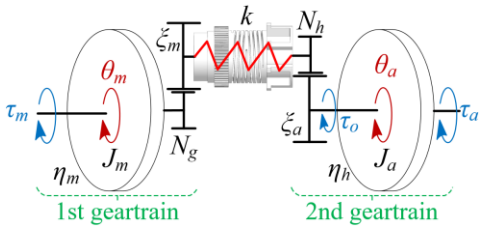

Fig. 3. Dynamic model of the actuator

The robotic actuator employed in this study was developed in [17] and serves as the hardware platform for evaluating the proposed LSTM-based torque estimation model. Its overall architecture is shown in Fig. 1, with a cutaway view in Fig. 1(a) and the internal transmission layout in Fig. 1(b). The assembled prototype, shown in Fig. 2, has an overall envelope of 165×176×121 mm³ and a total mass of 5.8 kg.

Motion is generated by a servo motor (ECM-A3L-CY0604RS1) fitted with a 24-bit absolute encoder. Rather than routing the motor output directly to the harmonic drive (SHD-40-50-2SH), a screw gear and belt drive redirect the transmission path to align with the harmonic drive axis, reducing the actuator's axial footprint. The belt drive and screw gear together form a combined gear ratio N_g, while the harmonic drive provides an additional ratio N_h, yielding a total reduction of N_gN_h from input to output.

The key mechanical component of this work is the compliant helical tube, shown in isolation in Fig. 2(c), which is inserted between the belt drive and the harmonic drive input. The tube is fabricated from heat-treated carbon steel and consists of three integrated subcomponents − a pulley, the helical flexure, and a mounting flange − with a measured torsional stiffness of 40.95 Nm/rad and a mass of 0.425 kg. Its hollow construction, with an inner diameter of 41 mm, allows the output shaft and any cabling to pass through the actuator centerline without affecting the overall form factor or adding to the actuator's footprint. Under torsional load, the tube undergoes measurable angular deformation that scales linearly with applied torque, providing a physically meaningful and encoder-measurable signal for learning-based estimation.

Three absolute encoders are embedded in the actuator to capture its kinematic state. The motor-integrated encoder measures the motor angle θ_m, a second encoder at the harmonic drive wave generator measures θ_w, and a third encoder at the rear of the actuator measures the output angle θ_a through the output shaft. From these three signals, two deformation quantities can be derived: the tube deformation from θ_m and θ_w, and the flex spline deformation from θ_w and θ_a. Because the compliant tube is substantially more flexible than the flex spline, its deformation is considerably larger and provides richer signal content for model training, making it the primary sensing feature in the proposed framework.

2.2 Modeling of the actuator

The dynamic model of the robotic actuator is shown in Fig. 3. The first geartrain includes the transmission components between the motor and the compliant tube, as illustrated in Fig. 1(b), where τ_m denotes the motor torque. The viscous damping coefficient and efficiency of the first geartrain are represented by ξ_m and η_m. The second geartrain consists of the

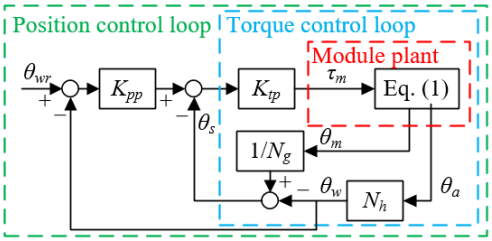

Fig. 4. Schematic diagram of the impedance controller

Table 1 Dynamic parameters of the actuator

$N_g = 2$, $N_h = 51$, $\xi_m = 0$ Nms/rad, $\eta_m = 1$, $\xi_a = 6.5$ Nms/rad, $\eta_h = 0.5$, $k = 40.95$ Nm/rad, $J_m = 9.9\times10^{-5}$ kgm^2, $J_a = 1$ kgm^2

transmission components from the compliant tube to the output, where τ_a denotes the external torque, and ξ_a and η_h represent the viscous damping coefficient and efficiency, respectively. The equivalent inertias of the first and second geartrains are denoted as J_m and J_a, respectively. The compliant tube with stiffness k connects the first and second geartrains. The governing equations of the actuator can be expressed as follows:

$$\begin{aligned} J_a\ddot{\theta}_a + \xi_a\dot{\theta}_a + \eta_h N_h k(N_h\theta_a - \theta_m/N_g) &= \tau_a \\ J_m\ddot{\theta}_m + \xi_m\dot{\theta}_m/N_g^2 + k(\theta_m/N_g - N_h\theta_a)/N_g &= \tau_m\eta_m \end{aligned} \quad (1)$$

where the term $\theta_m/N_g - N_h\theta_a$ represents the deformation of the total drivetrain, which includes the belt drive, the compliant tube, and the flex spline, as seen from the axis of the compliant tube. The deformation of the total drivetrain is indirectly computed from θ_a and θ_m and is also denoted as θ_{s1}. Since the stiffness of the compliant tube is much lower than those of the belt drive and flex spline, only the deformation of the compliant tube is considered.

The dynamic parameters of the robotic actuator are listed in Table 1. The total gear ratio from the actuator input to output, denoted as N_gN_h, is 102. The maximum output torque and speed are 292 Nm and 300°/s, respectively. When the motor applies the maximum torque, the compliant tube delivers maximum rotation of approximately ±8°, which remains within the allowable rotation range of the tube. Consequently, the full torque capacity of the motor can be effectively utilized.

In Table 1, the values of J_m and J_a were obtained using SolidWorks, whereas the values of ξ_a and η_h were determined experimentally. In contrast, the effects of ξ_m and η_m in the first geartrain are considerably smaller than those in the second geartrain. Therefore, the values of ξ_m and η_m were assumed to be 0 and 1, respectively.

2.3 Impedance control model of the actuator

Impedance control is widely adopted in robotic systems because it allows the actuator to exhibit varied interaction behaviors with the environment. High-impedance control is typically employed to achieve precise position tracking, while zero-impedance control is commonly used in teaching or demonstration modes, where minimal resistance to external forces is desired. Moreover, impedance control is an interaction-based, indirect force control strategy that specifies a target impedance between the actuator and the environment rather than directly commanding output forces. It can be formulated as a hybrid position–force control scheme, simultaneously regulating motion and interaction forces, thereby improving adaptability, safety, and robustness compared with pure position or torque control. The schematic of the impedance controller is shown in Fig. 4.

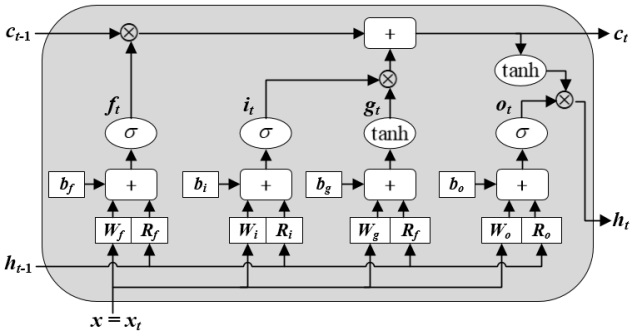

Fig. 5. Schematic of the LSTM network

The impedance controller includes a proportional gain K_{pp} and an inner torque controller, where K_{pp} can be tuned to modify the actuator's interaction impedance with the environment. The torque controller includes a proportional gain K_{tp} and the actuator system, as described in Eq. (1). In the experimental setup, the values of K_{pp} and K_{tp} were set according to the impedance mode. Under high-impedance control, $K_{pp} = 15$ and $K_{tp} = 5$; whereas under zero-impedance control, $K_{pp} = 0$ and $K_{tp} = 0.5$. Symbol θ_s denotes the deformation of the compliant tube, which is directly computed from θ_w and θ_m.

$$\theta_s = \theta_m/N_g - \theta_w \quad (2)$$

In Fig. 4, unlike conventional impedance control that relies on direct torque feedback, the deformation of the compliant tube is used as feedback. This deformation provides an indirect measure of output torque, enabling impedance control while remaining compatible with the torque controller.

III. LSTM-BASED TORQUE ESTIMATION FRAMEWORK AND DEEP LEARNING MODEL

3.1 Long short-term memory (LSTM) network

A long short-term memory network is a specialized class of recurrent neural network (RNN) that can capture long-term dependencies in sequential data. Unlike traditional RNNs, which suffer from limited memory and vanishing gradients [18], LSTMs use memory cells and gating mechanisms to selectively retain or discard information over extended time horizons. This ability makes LSTM more suitable for modeling dynamic systems with hysteresis.

As shown in Fig. 5, the LSTM network consists of a cell state $\boldsymbol{c_t}$ that serves as an internal memory, along with three primary gates: the input gate $\boldsymbol{i_t}$, forget gate $\boldsymbol{f_t}$, and output gate $\boldsymbol{o_t}$. These gates regulate the flow of information into, within, and out of the memory cell. The equations of the LSTM can be expressed as follows:

$$\boldsymbol{f_t} = \sigma(\boldsymbol{W_f x_t} + \boldsymbol{R_f h_{t-1}} + \boldsymbol{b_f}) \quad (3)$$

$$\boldsymbol{i_t} = \sigma(\boldsymbol{W_i x_t} + \boldsymbol{R_i h_{t-1}} + \boldsymbol{b_i}) \quad (4)$$

$$\boldsymbol{g_t} = \tanh(\boldsymbol{W_g x_t} + \boldsymbol{R_g h_{t-1}} + \boldsymbol{b_g}) \quad (5)$$

$$\boldsymbol{c_t} = \boldsymbol{f_t} \odot \boldsymbol{c_{t-1}} + \boldsymbol{i_t} \odot \boldsymbol{g_t} \quad (6)$$

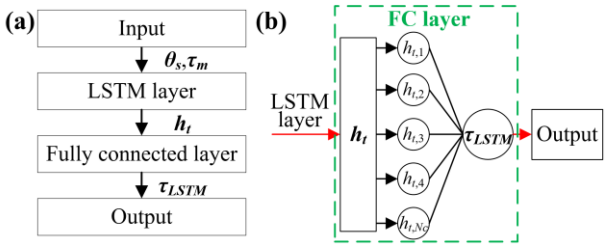

Fig. 6. Schematic of the (a) computational process and (b) the fully connected layer of the deep learning model

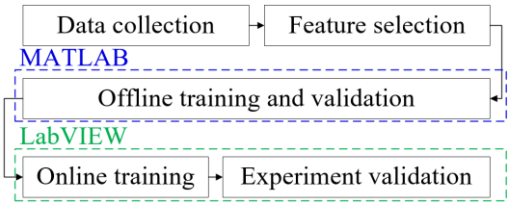

Fig. 7. Training process of the deep learning-based estimation model

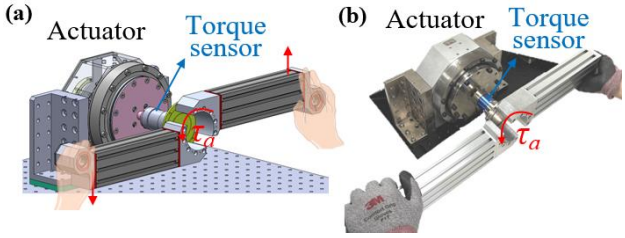

Fig. 8. Experimental setup of the deep learning model (a) CAD model and (b) physical prototype

$$\boldsymbol{o}_t = \sigma\left(\boldsymbol{W}_o \boldsymbol{x}_t + \boldsymbol{R}_o \boldsymbol{h}_{t-1} + \boldsymbol{b}_o\right) \tag{7}$$

$$\boldsymbol{h}_t = \boldsymbol{o}_t \odot \tanh(\boldsymbol{c}_t) \tag{8}$$

where $\boldsymbol{x}_t$ represents the input vector at time step t, $\boldsymbol{h}_t$ is the hidden state, $\sigma()$ denotes the sigmoid activation function. Symbol $\odot$ denotes element-wise (Hadamard) multiplication. In Eqs. (3), (4), (5), and (7), the weights $\boldsymbol{W}$ and $\boldsymbol{R}$ correspond to the input-to-hidden and hidden-to-hidden connections, respectively, with the subscripts indicating the gate to which they correspond. Symbol $\boldsymbol{b}$ denotes the corresponding bias vectors. The forget gate determines how much of the previous cell state $\boldsymbol{c}_{t-1}$ is retained, whereas the input gate $\boldsymbol{i}_t$ and candidate cell state $\boldsymbol{g}_t$ control the addition of new information. Finally, the output gate $\boldsymbol{o}_t$ modulates the information propagated from the current cell state to the hidden state.

The LSTM's gating mechanism enables the model to capture relevant temporal dependencies and learn the nonlinear, history-dependent dynamics of the system. For the torque estimation of the robotic actuator, the LSTM model can effectively capture hysteresis by processing sequential input features, such as the output angle, velocity, or compliant tube deformation.

3.2 Computational process of the deep learning model

This section describes the computational process of the deep learning model, applied in both offline and online stages. The model consists of the input, LSTM layer, fully connected layer, and output, as shown in Fig. 6(a).

The input provides the features required for training, such as θ_{s1}, θ_s, or τ_m. These features contain information about the actuator's state and operating conditions, and are crucial for capturing the actuator's nonlinear and hysteretic dynamics. The input features are fed into the LSTM layer for learning, and the resulting hidden states $\boldsymbol{h}_t$ are passed to the fully connected layer (FC layer), as shown in Fig. 6(b). The equations of the FC layer can be expressed as follows:

$$\tau_{LSTM,t} = \boldsymbol{W}_{FC}\boldsymbol{h}_t + b_{FC} \tag{9}$$

where $\boldsymbol{W}_{FC}$ and b_{FC} denote the weight and bias of the FC layer, respectively. The FC layer integrates the incoming features and maps them into a feature space suitable for torque estimation and finally outputs the estimated torque τ_{LSTM}.

During both online and offline training, the value of τ_{LSTM} is compared with the torque sensor (DYJN-104) value τ_{TS}. Model parameters such as weights and biases are iteratively updated to minimize the prediction error. This layer-wise architecture enables effective mapping from physical features to accurate torque estimations.

Table 2 Parameter settings of the deep learning model

Number of cells, N_c	250	Time step (s)	0.01
Length of sequence, L_s	200	Batch size	64
Train / Valid (%)	80 / 20	Epoch	3

Table 3 Input features of the deep learning model using different encoder sets

Types	Type I	Type II	Type III
Encoder set	Three-encoder (θ_m, θ_w, θ_a)	Dual-encoder (θ_m, θ_w)	Dual-encoder (θ_m, θ_a)
Input features	θ_s, τ_m, α_a	θ_s , τ_m	θ_{s1}, τ_m

3.3 Training process of the deep learning model

As illustrated in Fig. 7, the training process of the deep learning-based torque estimation model consists of five stages: data collection, feature selection, offline training and validation, online training, and experimental validation. In the data collection stage, the actuator was operated in impedance control mode, with a human operator applying external force to its output link to generate a torque τ_a, as shown in Fig. 8. Since the torque input was generated manually, the applied force was approximately periodic but varied across repetitions. This variability provides a realistic disturbance that can verify the accuracy of the proposed model under non-ideal conditions. The torque sensor value τ_{TS} and encoder readings were recorded for use as training data. Based on the actuator dynamics in Eq. (1), θ_s was selected because it indirectly reflects the output torque of the actuator, whereas τ_m, as the sole driving input of the actuator, provided additional dynamic information. These two features constituted the primary inputs to the deep learning model.

In the offline training stage, the LSTM-based model was trained with the collected dataset using the MATLAB deep-learning toolbox. The parameters of both the LSTM and FC layers were iteratively updated until the training loss converged. The main training parameters are summarized in Table 2. To evaluate the robustness of the model, K-fold cross-validation was employed, where the dataset was partitioned into K folds and the model's performance was averaged across folds to assess generalization. In each fold, the training and validation ratio was set to 80% and 20%,

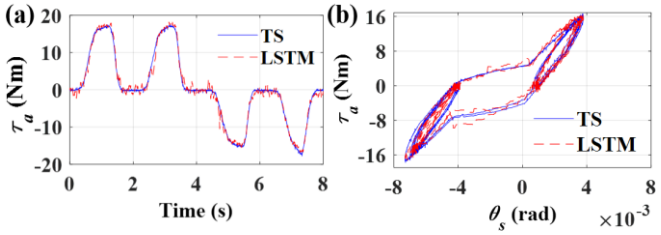

Fig. 9. (a) Torque estimation results and (b) hysteresis behavior with the Type I set

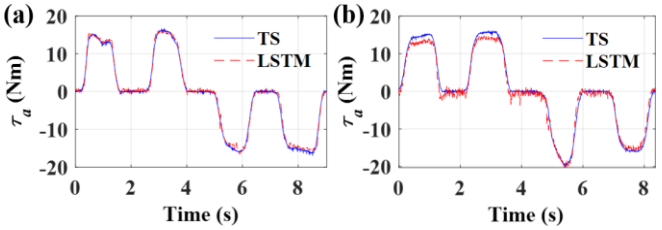

Fig. 10. Torque estimation results using (a) Type II and (b) Type III sets

Table 4 Torque estimation results for different encoder sets

Types	Type I	Type II	Type III
Input features	θ_s, τ_m, α_a	θ_s, τ_m	θ_{s1}, τ_m
RMSE (Nm)	0.9586	0.6578	1.3286
Error percentage (%)	5.46	3.96	7.48

respectively. Shapley additive explanations (SHAP) analysis was also performed to quantify the contribution of each selected feature. The parameters of the offline-trained model were deployed in a real-time LabVIEW environment for online training. In this stage, the estimation error between τ_{TS} and τ_{LSTM} was used to update the weights and biases of the FC layer, thereby refining the model for real-time operation. Experimental validation was conducted by deploying the final parameters obtained from the online training to verify the accuracy of the torque estimation model.

IV. Performance Analysis of the Torque Estimation Model with Different Encoder Sets

The proposed deep learning-based estimation model can be trained using different features extracted from the encoders. Table 3 summarizes three different feature sets: two from dual-encoder selection and one from a three-encoder selection. For Type I set, the output angular acceleration α_a, obtained by differentiating θ_a twice with respect to time, was added to improve the training of the torque estimation model.

The feasibility of the proposed torque estimation model was validated by training it with Type I set and testing it under high-impedance control, where the actuator remained nearly stationary and responded only to externally applied torques. The results are illustrated in Fig. 9. The estimated torques closely match the torque sensor measurements in Fig. 9(a). Fig. 9(b) shows that the hysteresis curve of the compliant tube is slightly biased, indicating an asymmetric response under cyclic loading. Despite this, the LSTM-based model accurately captures the overall behavior and is consistent with the torque sensor values. These results confirm the feasibility of the proposed torque estimation model.

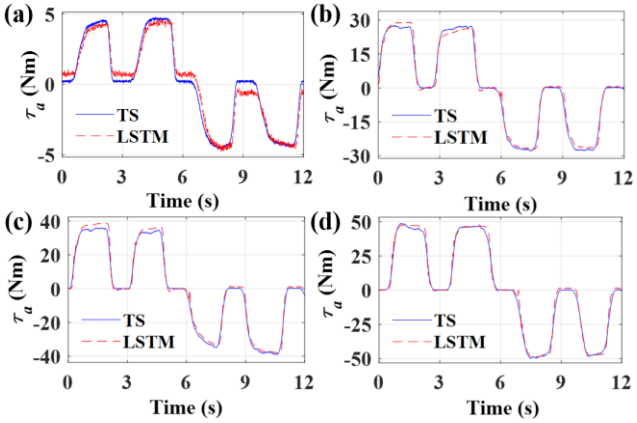

Fig. 11. Torque estimation results with different torque magnitudes (a) 5 Nm (b) 30 Nm (c) 40 Nm (d) 50 Nm (Type II set)

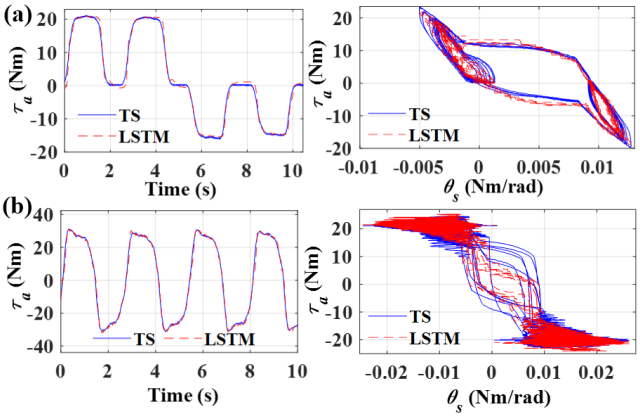

Fig. 12. Torque estimation results and hysteresis behavior under (a) high-impedance and (b) zero-impedance mode

To investigate the influence of different encoder sets on the torque estimation performance of the proposed estimation model, experiments were conducted using various input features derived from Type II and Type III sets. As shown in Fig. 10, the performance of Type II set is clearly superior to that of Type III set. This may be attributed to the actuator operating in high-impedance mode, where the output angle θ_a remains nearly stationary and varies only within a range close to the encoder sensor resolution, making torque estimation susceptible to noise. However, this noise can be effectively mitigated by filtering θ_{s1} during training.

The estimation results under high-impedance control for different encoder sets are summarized in Table 4. The error percentage was calculated by dividing each RMSE value by the maximum measured torque, providing a common basis to compare errors across different conditions. Type II set with θ_m and θ_w as input features exhibits the lowest root mean square error (RMSE), indicating the best torque estimation performance. Therefore, this feature set was adopted for all subsequent deep learning-based sensing experiments to ensure optimal performance.

V. Generalization of the Estimation Model

5.1 Estimation model with different external torques

In Sec. 4, the training and validation experiments were conducted within an externally applied torque range from 10

Table 5 Torque estimation results with different torque levels (type II feature set)

Applied torque (Nm)	5	20	30	40	50
RMSE (Nm)	0.5767	0.6578	1.7998	2.1240	2.5858
Error percentage (%)	10.92	3.96	5.53	4.49	4.79

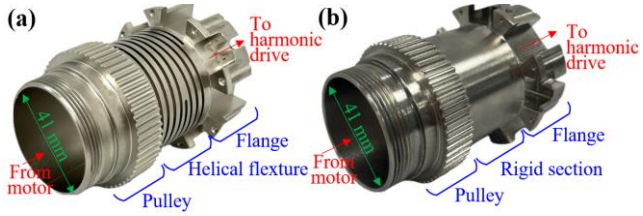

Fig. 13. (a) Soft tube (b) Rigid tube

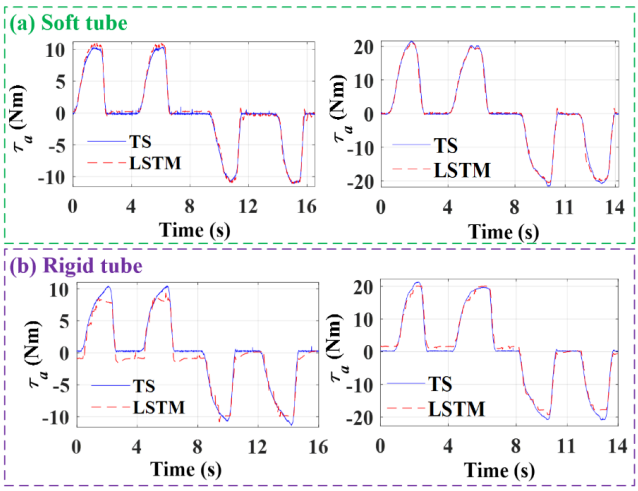

Fig. 14. Torque estimation results with (a) soft tube and (b) rigid tube

to 20 Nm. To further verify the generalization ability of the proposed torque estimation model, additional experiments were performed under both smaller and larger external torque conditions. In these tests, the actuator was operated in high-impedance mode with Type II set.

Fig. 11 shows the results under different applied torque magnitudes. The proposed model accurately captures the torque variations across the entire range of external torques. Even when the applied torque reaches as high as 50 Nm, the estimated torque remains closely aligned with the torque sensor values. The RMSE and error percentage results are summarized in Table 5. As the external torque increases, the RMSE gradually rises. Nevertheless, the error remains within 2.5858 Nm at 50 Nm, indicating that the proposed estimation model maintains high accuracy even under significantly larger external torques than those used during training. These results confirm that the torque estimation model, trained under limited torque conditions, can be effectively generalized to a wide range of external torques, thereby improving its robustness under unpredictable scenarios.

5.2 Torque estimation model with different impedance modes

To evaluate the generalization ability of the proposed torque estimation model under varying impedance conditions, experiments were conducted in both high-impedance and zero-impedance modes, which are commonly used in robotic applications. An additional input feature, the wave generator

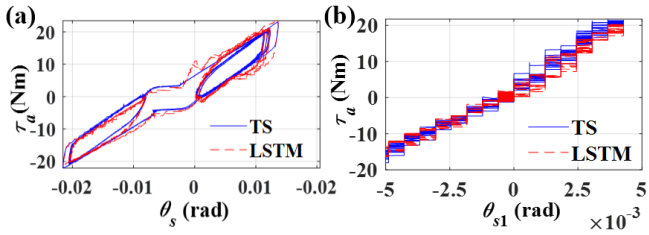

Fig. 15. Hysteresis behavior with the (a) soft tube and (b) rigid tube

Table 6 Torque estimation results of the estimation model with different connection tubes

Tubes	Soft	Stiff	Rigid
Stiffness (Nm/rad)	14.3	40.95	Nearly infinity
RMSE (Nm)	0.6660	0.6578	1.2496
Error percentage (%)	2.98	3.96	5.87

angular velocity ω_w, was added to Type II set to facilitate the estimation model distinguishing between zero-impedance and high-impedance behaviors. This allows the model to capture dynamic differences between the two control modes, particularly since the actuator operates at noticeable speeds under zero-impedance mode.

As shown in Fig. 12, the torque estimation results capture external torques accurately under both high-impedance and zero-impedance modes. The corresponding RMSE values were 1.1380 Nm and 1.8922 Nm, respectively. The corresponding error percentages were 5.38% and 5.63%, respectively. In addition, the high-impedance mode clearly exhibits the actuator's hysteresis behavior. However, under zero-impedance mode, the hysteresis behavior is influenced by the continuity and stability of the applied external torques, making it difficult to represent using fitting-based or logic-based methods. This highlights the necessity of employing a deep learning-based model for accurate torque estimation.

5.3 Torque estimation model with different tube stiffnesses

Three different tubes, as shown in Fig. 2(c) and Fig. 13, were applied in the actuator to evaluate the influence of tube stiffness on the torque estimation model. All tubes share the same overall dimensions; the only difference lies in the helical flexure geometry formed on the thin wall of the tube. The tube in Fig. 2(c) is denoted as the stiff tube, whereas the tubes in Figs. 13(a) and 13(b) are denoted as the soft tube and rigid tube, respectively. Different stiffnesses of the compliant tubes are achieved by altering the length of the helical flexures. Experiments were conducted using the soft tube (k = 14.3 Nm/rad), the stiff tube (k = 40.95 Nm/rad), and the rigid tube. For the stiff and soft tubes, the actuator was operated under the high-impedance mode using Type II set. For the rigid tube, the deformation θ_s is too small. Hence, Type III set is used for the rigid tube. Feature θ_{s1} can be used to estimate the deformation of the flex spline in the harmonic drive.

As shown in Fig. 10(a), Fig. 14, and Table 6, the soft and stiff tubes exhibited comparable estimation performance and both achieved substantially lower errors than the rigid tube. In addition, Fig. 15 illustrates the hysteresis behavior of the

compliant tubes and the rigid tube. It can be observed that the compliant tubes more clearly reveal the actuator's hysteresis characteristics, which is advantageous for constructing accurate estimation models using deep learning-based methods. By contrast, the rigid tube exhibited only small angular deformations, primarily arising from the flex spline, and these deformations were very close to the resolution limit of the external encoder. Consequently, the hysteresis behavior appeared discontinuous, and the model's estimation displayed non-smooth behavior. These results indicate the necessity of incorporating compliant tubes in actuators. The deformation of the compliant tubes provides salient input features for the learning model, thereby enhancing estimation accuracy compared to rigid tubes.

VI. Conclusions

This paper presented a torque estimation framework for harmonic drive actuators that integrates compliant tube deformation with a deep learning-based estimation model. Using encoder-derived features, the proposed LSTM network effectively captured nonlinear hysteresis and achieved robust torque estimation under diverse operating conditions. Experiments showed that the dual-encoder configuration achieved the lowest error of 3.96%, outperforming the three-encoder and alternative dual-encoder setups. Among compliant tube designs, the soft tube achieved the highest estimation accuracy. These results show that integrating mechanical compliance with learning-based models enables accurate, efficient, and sensorless torque estimation for compact, torque-controlled robotic systems.

References

[1] N. Kashiri, L. Baccelliere, L. Muratore, A. Laurenzi, Z. Ren, E. M. Hoffman, M. Kamedula, G. F. Rigano, J. Malzahn, S. Cordasco, P. Guria, A. Margan, and N. G. Tsagarakis, "Centauro: A hybrid locomotion and high power resilient manipulation platform," IEEE Robot. Autom. Lett., vol. 4, no. 2, pp. 1595–1602, 2019.

[2] S. Rader, L. Kaul, P. Weiner, and T. Asfour, "Highly integrated sensor-actuator-controller units for modular robot design," in Proc. IEEE Int. Conf. Adv. Intell. Mechatronics (AIM), Munich, Germany, 2017, pp. 1160–1166.

[3] M. Randazzo, M. Fumagalli, F. Nori, L. Natale, G. Metta, and G. Sandini, "A comparison between joint level torque sensing and proximal F/T sensor torque estimation: Implementation on the iCub," in Proc. IEEE/RSJ Int. Conf. Intell. Robots Syst. (IROS), San Francisco, CA, USA, 2011, pp. 4161–4167.

[4] H. Liu, S. Cui, Y. Liu, Y. Ren, and Y. Sun, "Design and vibration suppression control of a modular elastic joint," Sensors, vol. 18, no. 6, p. 1869, 2018.

[5] C. Irmscher, E. Woschke, E. May, and C. Daniel, "Design, optimisation and testing of a compact, inexpensive elastic element for series elastic actuators," Med. Eng. Phys., vol. 52, pp. 84–89, 2018.

[6] Y.-L. Yu and C.-C. Lan, "Design of a miniature series elastic actuator for bilateral teleoperations requiring accurate torque sensing and control," IEEE Robot. Autom. Lett., vol. 4, no. 2, pp. 500–507, 2019.

[7] C.-H. Huang, K.-W. Chiao, C.-P. Yu, Y.-C. Kuo, and C.-C. Lan, "A variable-stiffness robot for force-sensitive applications," IEEE/ASME Trans. Mechatronics, vol. 28, no. 4, pp. 1862–1870, 2023.

[8] J. de Gea Fernández, B. Yu, V. Bargsten, M. Zipper, and H. Sprengel, "Design, modelling and control of novel series-elastic actuators for industrial robots," Actuators, vol. 9, no. 1, p. 6, 2020.

[9] M. Cempini, F. Giovacchini, N. Vitiello, M. Cortese, M. Moisé, F. Posteraro, and M. C. Carrozza, "NEUROExos: A powered elbow orthosis for post-stroke early neurorehabilitation," in Proc. 35th Annu. Int. Conf. IEEE Eng. Med. Biol. Soc. (EMBC), Osaka, Japan, 2013, pp. 342–345.

[10] W. Yun, J. Kim, and S. Oh, "Novel series elastic actuator towards high torque capacity with high sensitive torque measurement," IEEE Robot. Autom. Lett., vol. 9, no. 6, pp. 5425–5432, 2024.

[11] Y. B. Kim, U. Kim, D.-Y. Seok, J. So, Y. H. Lee, and H. R. Choi, "Torque sensor embedded actuator module for robotic applications," IEEE/ASME Trans. Mechatronics, vol. 23, no. 4, pp. 1662–1672, 2018.

[12] D.-H. Lee, Y.-H. Kim, J. Collins, A. Kapoor, D.-S. Kwon, and T. Mansi, "Non-linear hysteresis compensation of a tendon-sheath-driven robotic manipulator using motor current," IEEE Robot. Autom. Lett., vol. 6, no. 2, pp. 1224–1231, 2021.

[13] L. Zhou, W. Chen, W. Chen, S. Bai, Z. Zhao, J. Wang, and H. Yu, "Hysteresis modeling and compensation of a rotary series elastic actuator with nonlinear stiffness," Rev. Sci. Instrum., vol. 92, no. 9, 2021.

[14] D. H. Kim and J. H. Oh, "Hysteresis modeling for torque control of an elastomer series elastic actuator," IEEE/ASME Trans. Mechatronics, vol. 24, no. 3, pp. 1316–1324, 2019.

[15] Y.-S. Song, H.-L. Huang, F. Liu, F.-F. Xi, D.-Y. Zhou, and B. Li, "Torque estimation for robotic joint with harmonic reducer based on deformation calibration," IEEE Sensors J., vol. 20, no. 2, pp. 991–1002, 2020.

[16] A. Zhu, Y. Tanaka, F. Rafeedi, and D. Hong, "Cycloidal quasi-direct drive actuator designs with learning-based torque estimation for legged robotics," in Proc. IEEE Int. Conf. Robot. Autom. (ICRA), Atlanta, GA, USA, 2025.

[17] C.-H. Huang and C.-C. Lan, "High-torque-capacity helical flexures for series elastic actuators," IEEE/ASME Trans. Mechatronics, vol. 30, no. 6, pp. 6038–6049, 2025.

[18] R. Pascanu, T. Mikolov, and Y. Bengio, "On the difficulty of training recurrent neural networks," in Proc. Int. Conf. Mach. Learn. (ICML), Atlanta, GA, USA, 2013, pp. 1310–1318.